Preferential concentration of inertial sub-Kolmogorov particles: The roles of mass loading of particles, Stokes numbers, and Reynolds numbers

Sholpan Sumbekova,[1,*] Alain Cartellier,[1,†] Alberto Aliseda,[2,‡] and Mickael Bourgoin[3,§]

[1]*Univ. Grenoble Alpes, CNRS, Grenoble INP*, LEGI, F-38000 Grenoble, France*
[2]*Department of Mechanical Engineering, University of Washington, Seattle, Washington 98195-2600, USA*
[3]*Univ. Lyon, Ens de Lyon, Univ. Claude Bernard, CNRS, Laboratoire de Physique, F-69342 Lyon, France*

Turbulent flows laden with inertial particles present multiple open questions and are a subject of great interest in current research. Due to their higher density compared to the carrier fluid, inertial particles tend to form high-concentration regions, i.e., clusters, and low-concentration regions, i.e., voids, due to the interaction with the turbulence. In this work we present an experimental investigation of the clustering phenomenon of heavy sub-Kolmogorov particles in homogeneous isotropic turbulent flows. Three control parameters are varied over significant ranges: $\mathrm{Re}_\lambda \in [170–450]$, $\mathrm{St} \in [0.1–5]$, and volume fraction $\phi_v \in [(2 \times 10^{-6})–(2 \times 10^{-5})]$. The scaling of clustering characteristics, such as the distribution of Voronoi areas and the dimensions of cluster and void regions, with the three parameters is discussed. In particular, for the polydispersed size distributions considered here, clustering is found to be enhanced strongly (quasilinearly) by Re_λ and noticeably (with a square-root dependence) with ϕ_v, while the cluster and void sizes, scaled with the Kolmogorov length scale η, are driven primarily by Re_λ. Cluster characteristic size $\sqrt{\langle A_c \rangle}$ scales up to $\approx 100\eta$, measured at the highest Re_λ, while void sizes $\sqrt{\langle A_v \rangle}$, scaled also with η, are typically twice as large as clusters at the same Re_λ ($\approx 200\eta$). The lack of sensitivity of the above characteristics to the Stokes number lends support to the sweep-stick particle accumulation scenario. The non-negligible influence of the volume fraction, however, is not considered by that model and can be connected with collective effects.

I. INTRODUCTION

Turbulent flows laden with inertial particles can be found in a broad range of engineering systems and geophysical phenomena. Droplets in clouds, cleaning sprays, aerosol pollutants, marine snow, and planetesimals are just a few examples of such flows. Unlike tracer particles, inertial particles do not follow the flow velocity, but rather have their own dynamics resulting from the complex interaction of the particle inertia, their gravitational settling velocity, and the fluid excitation across the continuous turbulent spectrum. The behavior of turbulent flows laden with inertial particles is an active field of theoretical, numerical, and experimental research. An important and unique aspect of inertial particles interacting with a turbulent background is their tendency to cluster, creating a inhomogeneous particle concentration field, a phenomenon known as preferential concentration. Although several mechanisms, such as the centrifugal expulsion of particles from the core of the eddies [1] or the sticking property of zero-acceleration points of the carrier flow [2,3], have been proposed to explain preferential concentration, no clear picture has emerged yet regarding the scaling and dominant parameters controlling the underlying physical processes at play. This lack of quantitative understanding considerably limits our capacity to build physical models to describe

---

*Institute of Engineering Univ. Grenoble Alpes; sholpan.sumbekova@legi.grenoble-inp.fr

†alain.cartellier@legi.grenoble-inp.fr

‡aaliseda@u.washington.edu

§mickael.bourgoin@ens-lyon.fr

and predict the phenomenon and its consequences, for instance, coalescence or evaporation and condensation of droplets, in practical situations. Empirical models are also difficult to develop as preferential concentration involves many ingredients whose specific roles have not been clearly identified yet: particle inertia, turbulence characteristics, gravitational settling, disperse phase volume fraction, etc. In this context, the present article reports a systematic experimental exploration of preferential concentration as several control parameters known to influence this phenomenon are varied over a wide range. These physical parameters can be related to several dimensionless parameters.

(i) Inertia is characterized by the particle Stokes number $St = \tau_p/\tau_\eta$, the ratio between the particle viscous relaxation time $\tau_p = \frac{1}{18}\frac{\rho_p}{\rho_f}\frac{D^2}{\nu}$ (where D is the drop diameter, ρ_p and ρ_f denote the particle and carrier fluid densities, respectively, and ν is the fluid's kinematic viscosity), and the dissipation time of the carrier turbulence $\tau_\eta = \sqrt{\nu/\epsilon}$ (where ϵ is the turbulent kinetic energy dissipation rate). For small particles [with diameter D much smaller than the dissipative scale of the flow $\eta = (\nu^3/\epsilon)^{1/4}$], the Stokes number can be related to the particle to fluid density ratio $\Gamma = \rho_p/\rho_f$ and to the ratio between the particle diameter D and the Kolmogorov microscale η as $St = \frac{(D/\eta)^2}{36}(1 + 2\Gamma)$. The Stokes number is therefore bounded in this analysis by the assumption of small particles ($D/\eta \ll 1$). Given a density ratio value (800 for water droplets in air), the Stokes number cannot be larger than 5 (for a maximum value of $D/\eta \approx 0.3$). Values of the Stokes number beyond this value represent finite-size particles that cannot be studied based only on the Stokes number, but require an independent measure of their finite size, as has been shown by the impact of finite-size neutrally buoyant particles on the turbulent characteristics of the carrier flow [4–10].

(ii) The strength of the turbulent excitation on the particles is related here to the Reynolds number of the carrier flow $Re = \sigma_u L/\nu$ (with σ_u and L equal to the velocity rms and the correlation length of the velocity fluctuations, respectively). In the present work we use the Reynolds number based on the Taylor microscale $R_\lambda = \sigma_u\lambda/\nu$, where the Taylor microscale λ is estimated as $\lambda = \sqrt{15\nu\sigma_u^2/\epsilon}$. Note that this estimate for R_λ is preferred to the commonly used relation $R_\lambda = \sqrt{15\,Re_L/C_\epsilon}$, where the dimensionless dissipation rate $C_\epsilon = \epsilon L/\sigma_u^3$ is assumed to be constant (independent of the geometry and Reynolds number), an assumption that may indeed not always be justified [11].

(iii) Gravitational settling is characterized by the Rouse number: the nondimensional ratio of the particle terminal velocity (taken as Stokes settling velocity in still fluid for $Re_p < 1$ particles) to the eddy velocity scale of the vortices that interact most strongly with the particles, in this case the Kolmogorov velocity [12–14]. This parameter represents the influence of the crossing trajectories effect [15,16] and preferential sweeping effect [1] on the interaction of inertial particles with the carrier turbulence. These interactions impact the settling rate of the particles as well as their clustering properties.

(iv) The overall concentration of the disperse phase in the flow is characterized by the volume fraction ϕ_v occupied by the particles. Volume fraction is known to impact particle-turbulence interactions at various levels. In dilute situations $\phi_v \leqslant 10^{-4}$, it is primarily the turbulence that affects the particles dynamics with no global modification of the properties of the turbulent carrier flow due to the presence of the particles: the one-way coupling regime. At higher volume fractions $10^{-4} < \phi_v < 10^{-3}$, two-way coupling effects emerge with a modification of the carrier turbulence due to the presence of the particles. At even higher disperse phase concentrations $10^{-3} < \phi_v$, four-way coupling mechanisms with additional particle-particle interactions appear. The volume fraction values used in the experiments are well within the dilute one-way coupling regime $\phi_v \leqslant 2 \times 10^{-5}$ and the mass loading is always less than 2%, so no significant modification of the turbulence in the carrier phase is considered.

Other parameters, such as polydispersity (in particle size and/or density) and particle shape anisotropy, can also influence clustering properties, but will not be addressed here.

As previously mentioned, although clear evidence of the effect of the control parameters studied here on clustering has been shown in experiments and simulations, a quantitative measure of the

impact of each of these parameters on preferential concentration over a wide range of values has not been obtained to date. For instance, available numerical studies (mostly carried out under the assumption of point particles [17]) and the few available experiments indicate that the Stokes number directly influences the clustering phenomenon, with a maximum degree of clustering for particles with $\mathrm{St} = O(1)$. Existing results also suggest that the clustering level increases with the increasing Reynolds number of the carrier flow [18]. Similarly, it was recently shown that the disperse phase volume fraction has a nontrivial effect on clustering [19], with a nonlinear dependence of the accumulation within clusters with the global concentration (even in situations of one-way coupling, where no global modulation of the carrier turbulence is expected due to the presence of the particles). Aliseda *et al.* [14] have also shown that gravitational settling is nontrivially connected to the preferential concentration phenomenon and to the global volume fraction and can be collectively enhanced within clusters. Better insight into such behaviors is required in order to clearly disentangle the role of the Stokes number, Reynolds number, and volume fraction and eventually start paving the way towards possible strategies to develop predictive and accurate models of preferential concentration.

One of the difficulties in characterizing the specific role of these parameters unequivocally lies in the practical complexity of systematically disentangling each parameter's contributions in actual experiments. For instance, for a given class of particles (with fixed size and density), varying the Reynolds number of the carrier flow (for instance, by reducing the viscosity ν of the fluid or increasing the energy dissipation rate ϵ) also results in a change of the particle Stokes number [as the dissipation scale $\eta = (\nu^3/\epsilon)^{1/4}$ and hence the ratio $\Phi = D/\eta$ also varies]. Similarly, even if the volume fraction ϕ_v is varied within the one-way coupling regime ($\phi_v \leqslant 10^{-5}$), the concentration within clusters may increase due to preferential concentration, inducing subtler particle-turbulence and particle-particle interactions, which in turn may result in nontrivial collective dynamics of particles and of clusters of particles that are out of reach for the commonly used point-particle models.

We present an experimental investigation of preferential concentration of water droplets in homogeneous isotropic turbulence turbulence generated by an active grid, where St, R_λ, and ϕ_v have been varied independently within a wide range of experimental available values. We report the influence of these parameters on the degree of preferential concentration based on Voronoi tessellation analysis [19,20] and on the cluster and void geometry. The article is organized as follows. Section II presents the experimental facility and the strategy to explore the ($\mathrm{St}, R_\lambda, \phi_v$) parameter space. Section III details the Voronoi tessellation method and proposes strategies to better handle possible biases in this analysis due to illumination inhomogeneity in the experiment. In Sec. IV we report the main results of this investigation, before proposing a detailed discussion in Sec. V, with conclusions and future lines of research identified from this work.

II. EXPERIMENTAL SETUP

Experiments were conducted in a wind tunnel with a test section of $0.75 \times 0.75 \times 4$ m^3 (see Fig. 1). Homogeneous isotropic turbulence is produced with an active grid located at the entrance of the test section. The mean streamwise velocity U in the wind tunnel was varied in the range $U \in 2.5$–10 m/s (corresponding turbulence properties are given below in Table I). Water droplets are injected 15 cm downstream of the active grid using an array of 18 pressure injection nozzles supplied with a controlled flow rate of water via a high-pressure pump. Three injector sizes (with different orifice diameters $D_{\mathrm{inj}} = 0.3$, 0.4, and 0.5 mm) were used to vary the size distribution of droplets injected in the flow. The droplet volume fraction can be further controlled by varying the flow rate of water F_{water} injected, which in our experiment evolves in the range $F_{\mathrm{water}} \in 0.8$–$1.9$ l/min. Overall, the combination of the three control parameters ($U, D_{\mathrm{inj}}, F_{\mathrm{water}}$) allows us to explore the parameter space ($\mathrm{St}, R_\lambda, \phi_v$). The main properties of the carrier turbulence, the seeded water droplets, and the accessible parameter space are described in the following section.
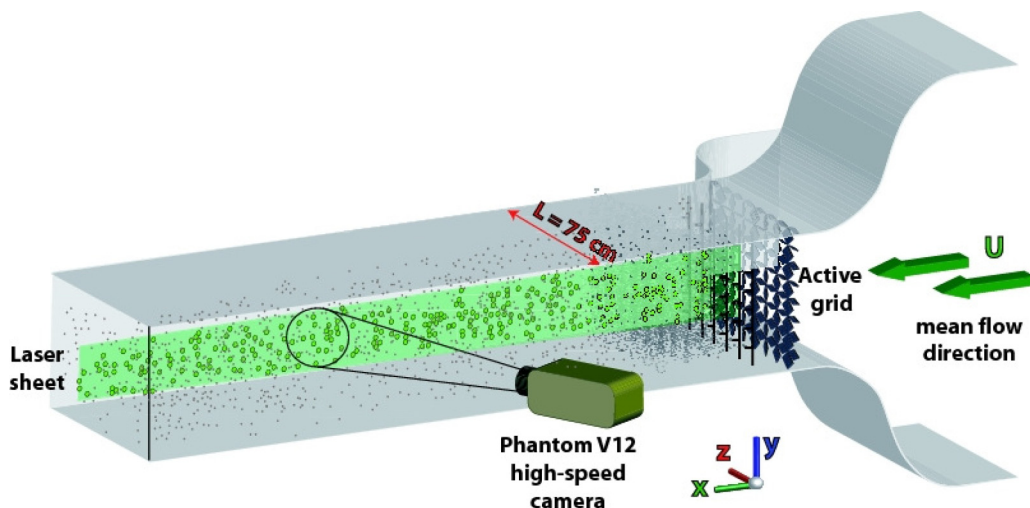
FIG. 1. Schematic view of the experimental facility.

A. Turbulence generation

The details of the active grid in the wind tunnel have been published in [18]. Briefly, it is made up of eight vertical and eight horizontal shafts on which square wings are mounted. Each axis is controlled individually by a stepper motor, so the solidity of the grid can be actively and dynamically changed. This turbulence generation technique was first introduced by Makita and Sassa [21] and has been reproduced in multiple studies in the literature (see, e.g., [22,23]). When a random forcing protocol

TABLE I. Conditions of the experimental runs.

| D (mm)	F_{water} (l/min)	U (m/s)	u' (m/s)	η (μm)	τ_η (s)	ϵ (m^2/s^3)	D_{max} (μm)	$\sigma(D)$ (μm)	D_{32} (μm)	$St_{D_{max}}$	St_{max}	ϕ_v ($\times 10^{-4}$)	Re_λ
0.3	0.8	2.36	0.30	431	0.011	0.20	35	17	60	0.3	0.26	0.09	200
0.3	0.8	4.11	0.59	250	0.004	1.35	32	19	61	0.7	0.5	0.05	300
0.3	0.8	6.42	1.00	162	0.002	6.12	24	18	60	1.0	0.29	0.03	400
0.3	0.8	9.19	1.49	114	0.001	20.73	37	18	58	5.0	2.3	0.02	490
0.3	1.2	2.37	0.33	429	0.011	0.21	21	17	52	0.1	0.05	0.14	240
0.3	1.2	4.03	0.62	255	0.004	1.26	27	17	59	0.5	0.17	0.08	350
0.3	1.2	5.95	0.92	174	0.002	4.74	24	17	57	0.9	0.22	0.06	390
0.3	1.2	8.85	1.41	118	0.001	18.27	28	16	57	2.7	2.15	0.04	470
0.4	1.9	2.32	0.32	439	0.012	0.19	36	19	62	0.3	0.2	0.22	240
0.4	1.9	3.95	0.56	260	0.004	1.17	45	20	65	1.4	0.68	0.13	290
0.4	1.9	5.95	0.95	174	0.002	4.74	32	20	66	1.6	0.42	0.09	420
0.4	1.9	8.64	1.40	121	0.001	16.83	30	20	69	2.8	0.77	0.06	480
0.4	1.4	4.07	0.59	252	0.004	1.31	26	21	66	0.5	0.19	0.10	300
0.4	1.4	6.27	1.00	166	0.002	5.64	28	21	67	1.4	0.94	0.06	420
0.4	1.4	8.82	1.43	118	0.001	18.02	29	20	66	2.7	1.84	0.04	480
0.5	1.9	2.30	0.30	442	0.012	0.19	23	23	67	0.1	0.05	0.23	200
0.5	1.9	4.13	0.58	249	0.004	1.37	32	23	72	0.8	0.4	0.13	290
0.5	1.9	6.16	0.96	168	0.002	5.32	37	22	70	2.3	1.02	0.08	400
0.5	1.9	8.68	1.40	120	0.001	17.05	33	21	70	3.5	2.3	0.06	480
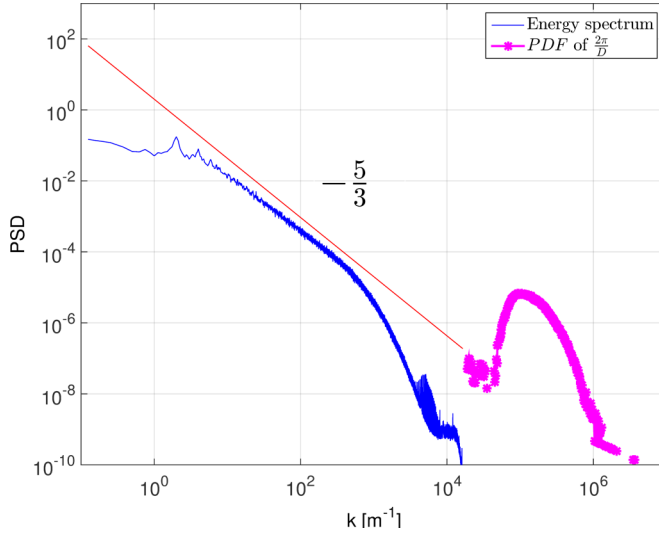
FIG. 2. Typical Eulerian energy spectrum of velocity fluctuations produced downstream of the active grid, obtained from classical hot-wire anemometry at the position where the water droplet's preferential concentration is investigated (3.5 m downstream of the grid). The typical distribution of $2\pi/D$, where D is the droplet diameter, shown in magenta on this graph (with arbitrary units on the ordinate axis), demonstrates that all droplets are indeed smaller than the Kolmogorov length scale.

is used to drive the rotation of the shafts and flapping of the wings, it generates stronger turbulence than a passive grid (turbulence intensity in our active grid flow is of the order of 15%–20%, while it is typically 2%–4% in passive grid wind-tunnel turbulence) while keeping good homogeneity and isotropy. It is worth mentioning that in spite of this high fluctuation level, active grid generated turbulence is often characterized using hot-wire anemometry under a frozen field Taylor hypothesis. We follow here the usual procedure, although it will be interesting in further studies (beyond the scope of the present work) to actually quantify the validity of the Taylor approximation in this situation. Figure 2 shows a typical spectrum (measured with classical hot-wire anemometry) of the carrier flow velocity fluctuations for $U = 10$ m/s, where a well-defined inertial range can be clearly identified over about two decades in wave-number space. We note that two small peaks can be seen in the lower-frequency part of the spectrum. The first peak is related to the rotation rate of the flaps of the active grid (which randomly varies in the range 1–3 Hz). The second peak is the first harmonic. In terms of spatial scales, using Taylor's hypothesis, the first peak corresponds to scales in the range 0.8–2.5 m for the lowest investigated velocity ($U \approx 2.5$ m/s) and to scales in the range 3.3–10 m for the highest explored velocity ($U \approx 10$ m/s). The second peak (first harmonic) represents spatial scales equal to one-half those given for the main frequency. Therefore, these peaks correspond to modulations of the carrier velocity field at wavelengths above 0.40 m in the worst-case scenario and above 1 m for the highest velocities explored. This is significantly larger than the region explored in the present study, which focuses on clustering properties at inertial scales (our measurement volume is of the order of 7 cm in its larger dimension), and such large-scale behavior is beyond the scope of the present work, although it may have an impact on large-scale clustering properties (such as superclustering [24]). Table I summarizes the main properties of the turbulence and the disperse phase, for the different values of mean stream velocity U.

B. Generation of water droplets

The 18 spray nozzles for water injection are fixed on 8 vertical bars at the same positions in the cross section as the vertical bars of the active grid, in order to minimize the flow disturbance
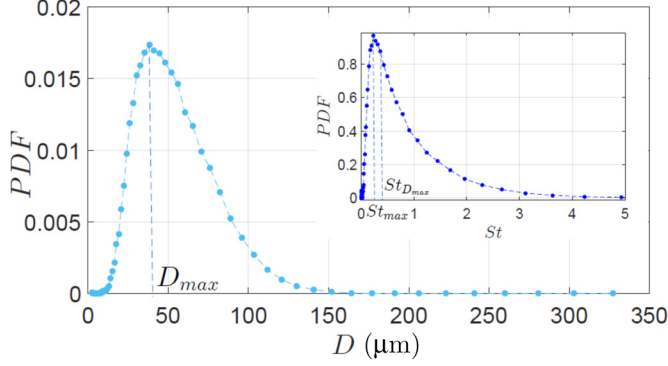
FIG. 3. Typical diameter distribution of water droplets in the wind tunnel (produced by the 0.4-mm injectors at a flow rate of 1.9 l/min). The inset shows the corresponding distribution of Stokes numbers for $R_\lambda = 172$. Dashed lines indicate the Stokes number defined on the most probable diameter and the most probable Stokes number.

due to the injector array. Hot-wire anemometry shows that the presence of the injector array does not modify the turbulence properties at the measurement location (3.5 m downstream of the grid); the turbulence spectra with and without injectors are undistinguishable. The size distribution of the droplets is controlled by the injector orifice size ($D_{\mathrm{inj}} = 0.3, 0.4$, and 0.5 mm) and depends only weakly on the flow rate F_{water}. Thus, the volume fraction ϕ_v was varied with a combination of four different liquid flow rates and four different wind-tunnel speeds, for a range of $2 10^{-6}$–$2 10^{-5}$, without significantly affecting the droplet mean size, which was varied independently. The ranges of dimensional and nondimensional parameters spanned in the experiments are shown in Fig. 4.

1. Droplet Stokes number

Figure 3 shows a typical size distribution of water droplets obtained from phase Doppler interferometry (PDI) measurements. The spray is strongly polydispersed, with a well-defined most-probable diameter. The droplet size distributions have been measured using PDI for all experimental conditions considered. The most-probable diameter D_{max}, the Sauter mean diameter D_{32}, and the standard deviation $\sigma(D)$ are reported in Table I. The most probable diameter evolves in a narrow range, from 21 to 45 μm. Otherwise, all conditions exhibit a comparable degree of polydispersity as $\sigma(D)/D_{32} = 0.31 \pm 10\%$ and $\sigma(D)/D_{\mathrm{max}} = 0.66 + (50\%\text{--}30\%)$. The inset in Fig. 3 represents the distribution of droplet Stokes numbers corresponding to the size distribution shown. A reference Stokes number for each experimental condition is defined using the most probable droplet diameter D_{max} in the distribution. Thus, for each experimental condition, the most representative particle Stokes number is estimated as $\mathrm{St}_{D_{\mathrm{max}}} = \frac{D_{\mathrm{max}}/\eta)^2}{36}(1 + 2\Gamma)$, with $\Gamma = \rho_{\mathrm{water}}/\rho_{\mathrm{air}} \simeq 830$. Alternative choices are possible. For example, one may also refer to the most-probable Stokes number $\mathrm{St}_{\mathrm{max}}$ (see the inset in Fig. 3) that slightly differs from the Stokes number based on D_{max}. For the experimental conditions explored here, the difference between the most-probable $\mathrm{St}_{\mathrm{max}}$ and $\mathrm{St}_{D_{\mathrm{max}}}$ based on D_{max} varies between 12% and 75% (see Table I). As pointed out earlier, since St depends on both D and η, for a given droplet distribution the Stokes number varies with the flow Reynolds number. Thus, St is sensitive to both wind-tunnel speed and injector orifice size as experimental controls.

2. Droplets volume fraction

The volume fraction ϕ_v of the droplet disperse phase in the wind tunnel is given by the ratio between the water flow rate F_{water} through injector array and the total flow rate of air and water across the tunnel cross section $F_{\mathrm{tot}} = F_{\mathrm{air}} + F_{\mathrm{water}}$ with $F_{\mathrm{air}} = SU$ where $S = (0.75 \text{ m})^2 \simeq 0.56 \text{ m}^2$
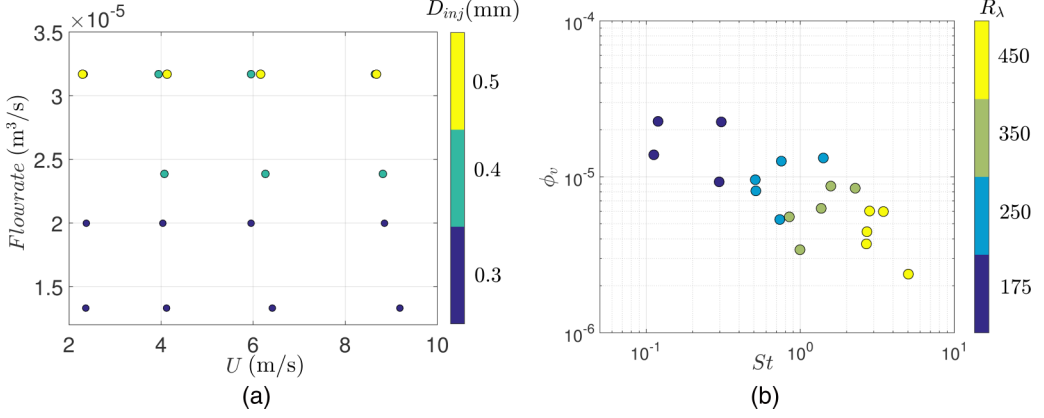
FIG. 4. (a) Map of control parameters explored. (b) Corresponding map of experimental parameter space.

is the area of the tunnel cross section: $\phi_v = \frac{F_{\text{water}}}{F_{\text{tot}}}$. Note that in all experiments $F_{\text{water}} < 2\,\mathrm{l/min}$ while $F_{\text{air}} > 1.4\,\mathrm{m}^3/\mathrm{s} \gg F_{\text{water}}$, so $F_{\text{tot}} \simeq F_{\text{air}}$ and $\phi_v \simeq \frac{F_{\text{water}}}{F_{\text{air}}} = \frac{F_{\text{water}}}{SU}$. Therefore, the volume fraction ϕ_v depends on both the liquid injection flow rate and the wind-tunnel mean speed.

C. Parameter space

The previous discussion shows the difficulty of independently varying the three parameters studied in this work $(\mathrm{St}, R_\lambda, \phi_v)$, as they are sensitive to changing more than one experimental control parameter $(U, D_{\text{inj}}, F_{\text{water}})$. By independently varying the injector diameter, the liquid phase flow rate and the mean wind-tunnel speed, the present study explores the parameter space $(\mathrm{St}, R_\lambda, \phi_v)$ (see Fig. 4) in the range $\mathrm{St} \in [0.1, 5]$, $R_\lambda \in [170, 460]$, and $\phi_v \in (2 \times 10^{-6})$–$(2 \times 10^{-5})$. Figures 4(a) and 4(b) represent the experimental parameters and the nondimensional control parameters that were accessible in the experiments.

By taking advantage of the experimental parameters that modified primarily one nondimensional number with no or weak influence on the other two, the influence of one parameter could be investigated, tracing horizontal or vertical lines in Fig. 4(b). Thus, the effect of the Stokes number (horizontal lines) can be studied, keeping a relatively constant volume fraction and with a moderate variation of Reynolds number. Similarly, the effect of volume fraction (vertical lines) can be teased out while keeping the Stokes and Reynolds numbers to small variations. Two sets of experimental conditions yielded almost identical Stokes number and volume fraction while changing the Reynolds number by 50%, hence allowing a limited exploration of the effect of Reynolds number.

D. Visualization of particle locations and time-resolved trajectories

The particles in the flow are illuminated by a laser sheet along the streamwise-vertical directions, at the midplane of the test section (Fig. 1). The thickness of the laser sheet is $\approx 1\,\mathrm{mm}$, or a few η. Because of the Gaussian profile of the laser beam, the illumination is inhomogeneous in the vertical direction (a slight inhomogeneity also exists in the horizontal direction, mostly due to sheet formation near the waist of the laser). Therefore, the laser intensity is maximum at midheight. Sequences of images are recorded using a high-speed camera (Phantom V12, Vision Research Inc., Wayne, NJ). A 105-mm Nikon macrolens on a Scheimpflug mount was used to visualize the laser sheet in forward-scattering conditions, improving the brightness of the droplets while keeping good focusing conditions over the entire image. The dimensions of the visualization area are $\simeq 10 \times \simeq 7\,\mathrm{cm}^2$ (covering a significant fraction of the integral scale of the carrier turbulence, which is of the order of $L_{\text{int}} \approx 15\,\mathrm{cm}$). For each experimental condition, defined by one triplet $(\mathrm{St}, R_\lambda, \phi_v)$ in the parameter
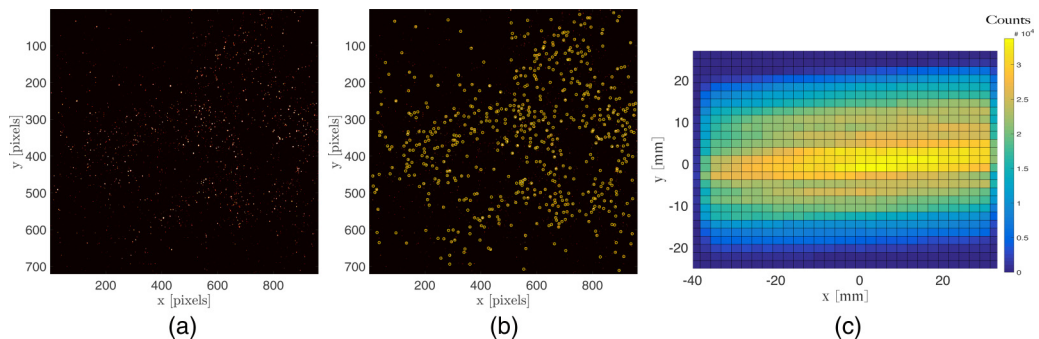
FIG. 5. (a) Typical raw image, (b) detected particles, and (c) probability of detected particles. The large-scale inhomogeneity of the detection reflects the Gaussian intensity profile in the laser illumination.

space in Fig. 4, we recorded 20 movies at full resolution (1280×800 pixels) at an acquisition rate of 2600 frames per second; the duration of each movie is ≈ 3.27 s (8500 frames). The high frame rate was selected to enable particle tracking between consecutive images. The number of particles per image typically ranges between 500 and 2000 depending on flow conditions.

The measurement location is 3.5 m downstream the injection of the droplets, where turbulence is fully developed and sufficiently far away from the injection location for cluster formation to have reached a stationary state. The time required for clusters to form is indeed not well understood. If we consider the duration of transients observed in direct numerical simulations as an estimate, two options are available: either transients are of the order of the integral time scale T_{int} of the carrier turbulence (provided the particle response time is much smaller than T_{int} [12], as is the case in this study) or they depend on a combination of turbulent and particle characteristic time scales. For instance, Yang and Lei [13] proposed 8 times the dissipation time scale τ_η plus 5 times the particle viscous realization time scale τ_p. In all our experimental conditions, the transit time of droplets between the injection plane and the measurement location ranges from 60 to 600 particle response times, or several integral time scales (from 1.8 to 2.5). Thus, particle residence times in the turbulence are expected to be long enough for clusters to be have reached equilibrium.

III. VORONOI TESSELLATION ANALYSIS

Voronoi tessellations, which have been proven to be a good estimator to quantify the clustering of particles [18–20,25–27], are used to diagnose the appearance and the strength of preferential concentration.

Illumination inhomogeneity correction

Illumination inhomogeneity, shown above in Fig. 5(c), requires additional image processing to calibrate the particle detection prior to diagnosing preferential concentration. As a consequence of the Gaussian intensity profile across the laser plane, particles are statistically more probable to be detected in the center of the visualization domain. Figure 5(a) shows an example of a raw recorded image and Fig. 5(b) indicates the corresponding particle detection. The map of probability of particle detection [Fig. 5(c)] clearly shows that particles are more likely to be detected in the center of the image. Analyzing the clustering properties of particles in such conditions, without calibration, may lead to errors in the diagnosis of the existence of clustering, simply due to the illumination bias. To prevent such a bias, previous studies have cropped images [18], limiting the analysis to the central region, where illumination is relatively homogeneous. Doing so, however, requires many more images for statistical convergence of the analysis and also biases the cluster or void analysis, as large structures cannot be detected. We use an alternative approach, allowing the use of the full image
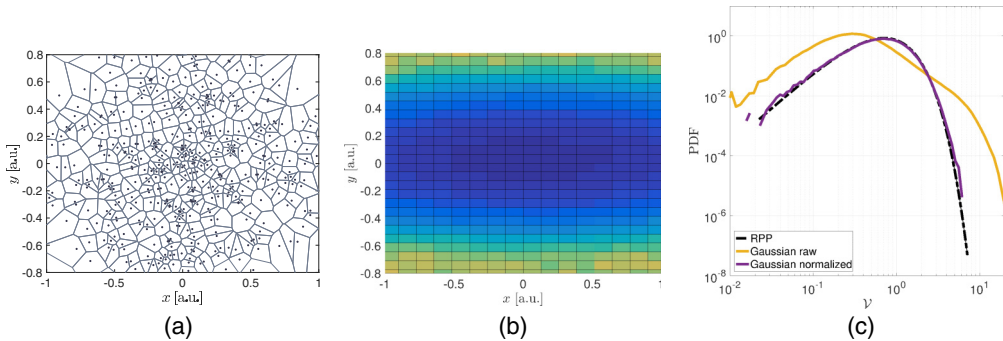
FIG. 6. (a) Example of randomly distributed particles, with a centered large-scale Gaussian modulation of the probability of particle locations (particles are more likely to be detected near the center than near the image edges), mimicking the experimental illumination nonhomogeneity due to the Gaussian profile of the laser sheet. (b) Coarse-grained field of the average local Voronoi area $\mathcal{A}_{\mathrm{mean}}(x,y)$, estimated from 1000 realizations as in (a). (c) PDF of Voronoi areas, estimated from 1000 synthetic images (with a few hundred particles in each image) for a random homogeneous RPP reference situation (black dashed line), a random but nonhomogeneous distribution as illustrated in (a) (yellow solid line), and the same random nonhomogeneous distribution where Voronoi areas are locally corrected by the contraction field $\mathcal{A}_{\mathrm{mean}}(0,0)/\mathcal{A}_{\mathrm{mean}}(x,y)$ shown in (b) (purple solid line).

with an appropriate correction to undo the bias in the estimation of the area of Voronoi areas where illumination is nonhomogeneous. A corrective local *contraction* factor is applied to the raw Voronoi cells in regions with lower illumination to correct for them being statistically larger. We illustrate the method using a synthetically generated random distribution of particles with a smooth Gaussian modulation. Figure 6(a) represents a realization of the synthetically generated particle field. Particles are randomly distributed following random Poisson process (RPP) distribution, but with a large-scale Gaussian modulation mimicking the experimental bias in the center of the images. Figure 6(c) shows that, although no clustering mechanism is present, the probability distribution function (PDF) of normalized Voronoi areas $\mathcal{V} = \mathcal{A}/\langle\mathcal{A}\rangle$ deviates significantly from the RPP case, simply because of the large-scale modulation of the probability of particle location. The standard deviation of $\mathcal{V}$ is $\sigma_{\mathcal{V}} \simeq 1.5 > \sigma_{\mathcal{V}}^{\mathrm{RPP}} = 0.53$. To correct this bias, the coarse-grained field of the local average Voronoi area $\langle\mathcal{A}(x,y)\rangle/\langle\mathcal{A}(0,0)\rangle$ [Fig. 6(b)] is estimated from an ensemble of 1000 realizations. The color of each rectangular zone in Fig. 6(b) represents the average value of the Voronoi area of particles detected within that zone. For smooth and large-scale inhomogeneities, the number of zones used for the coarse-grained field is not a critical parameter. This coarse-grained field is then used as a contraction factor, normalized to be maximum and equal to one where the particle probability is maximum, so the Voronoi area $\mathcal{A}$ of a particle $\mathcal{P}$, detected at a position (x,y), is corrected to become $\mathcal{A}^* = \mathcal{A}\langle\mathcal{A}(0,0)\rangle/\langle\mathcal{A}(x,y)\rangle$. The PDF of the corrected Voronoi areas $\mathcal{V}^* = \mathcal{A}^*/\langle\mathcal{A}^*\rangle$ is shown in Fig. 6 and found to exactly match the reference RPP PDF, proving that the calibration with this correction method effectively removes the bias. This procedure is used to unbias the Voronoi area statistics from the experimental images.

IV. RESULTS

A. Deviation from randomness of the particle concentration field: Standard deviation σ_v of the Voronoi area distributions

Figure 7 represents a typical Voronoi diagram from an experimental image. Colored structures represent detected clusters, further discussed below. Thousands of such tessellations are obtained for each experimental condition. Pair distribution functions of normalized corrected Voronoi areas are shown in Fig. 8(a), where the departure from the RPP case can be clearly observed. Figure 8(c)
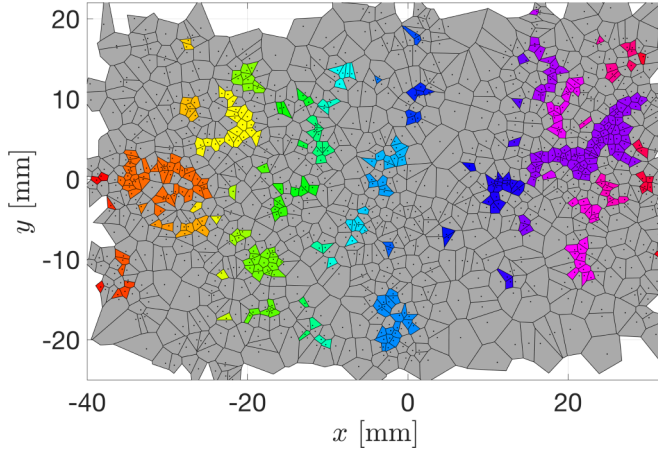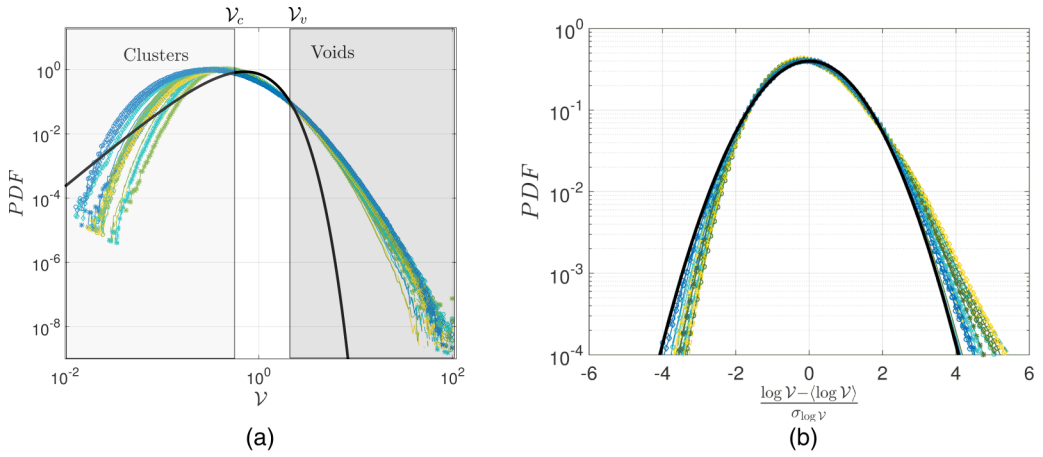
FIG. 7. Example of Voronoi diagram for one typical image of our experiment. Colored regions indicate clusters, defined following the procedure described in Sec. IV C.

$St = 0.3, R_\lambda = 200, \phi_v = 0.9 \times 10^{-5}$	
$St = 0.7, R_\lambda = 300, \phi_v = 0.5 \times 10^{-5}$	
$St = 1.0, R_\lambda = 400, \phi_v = 0.3 \times 10^{-5}$	
$St = 5.0, R_\lambda = 490, \phi_v = 0.2 \times 10^{-5}$	
$St = 0.1, R_\lambda = 240, \phi_v = 1.4 \times 10^{-5}$	
$St = 0.5, R_\lambda = 350, \phi_v = 0.8 \times 10^{-5}$	
$St = 0.9, R_\lambda = 390, \phi_v = 0.6 \times 10^{-5}$	
$St = 2.7, R_\lambda = 470, \phi_v = 0.4 \times 10^{-5}$	
$St = 0.3, R_\lambda = 240, \phi_v = 2.2 \times 10^{-5}$	
$St = 1.4, R_\lambda = 290, \phi_v = 1.3 \times 10^{-5}$	
$St = 1.6, R_\lambda = 420, \phi_v = 0.9 \times 10^{-5}$	
$St = 2.8, R_\lambda = 480, \phi_v = 0.6 \times 10^{-5}$	
$St = 0.5, R_\lambda = 300, \phi_v = 1.0 \times 10^{-5}$	
$St = 1.4, R_\lambda = 420, \phi_v = 0.6 \times 10^{-5}$	
$St = 2.7, R_\lambda = 480, \phi_v = 0.4 \times 10^{-5}$	
$St = 0.1, R_\lambda = 200, \phi_v = 2.3 \times 10^{-5}$	
$St = 0.8, R_\lambda = 290, \phi_v = 1.3 \times 10^{-5}$	
$St = 2.3, R_\lambda = 400, \phi_v = 0.8 \times 10^{-5}$	
$St = 3.5, R_\lambda = 480, \phi_v = 0.6 \times 10^{-5}$	

FIG. 8. (a) PDF of the corrected normalized Voronoi areas $\mathcal{V}$ for all experiments. The solid black line shows the RPP distribution. (b) Centered normalized PDF of $\ln(\mathcal{V})$ (decimal logarithm). The solid black line shows a Gaussian distribution with variance 1.
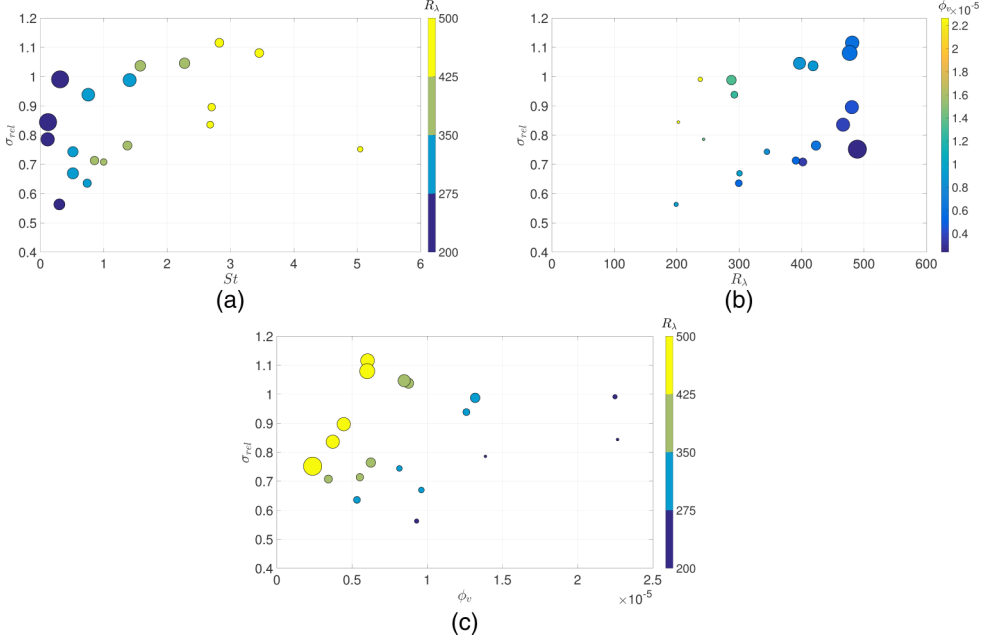
FIG. 9. (a) Standard deviation σ vs St. Symbol colors represent the Reynolds number, while the size of the symbols encodes the volume fraction (larger symbols correspond to experiments at larger volume fraction). (b) Standard deviation σ vs Re_λ. Symbol colors indicate the volume fraction, while the size of the symbols encodes the Stokes number (larger symbols correspond to experiments with larger Stokes numbers). (c) Standard deviation σ vs ϕ_v. Symbol colors reflect the Reynolds number, while the size of symbols encodes the Stokes number (larger symbols correspond to experiments with particles at larger Stokes number).

shows the PDF of $\ln(\mathcal{V})$ (decimal logarithm, centered by the mean and normalized by the standard deviation), emphasizing the quasi-log-normal distribution of the statistics of Voronoi areas, as previously reported [18,19]. This quasi-log-normality justifies the idea that the statistics of $\mathcal{V}$ can be described by a single parameter (recall that $\langle \mathcal{V} \rangle = 1$ by construction), generally the standard deviation of $\mathcal{V}$, $\sigma_\mathcal{V}$, to quantify the departure from the RPP distribution.

Figure 9 represents the difference between the experimental $\sigma_\mathcal{V}$ and the RPP value [$\sigma_{\mathrm{rel}} = (\sigma_\mathcal{V} - \sigma_\mathcal{V}^{\mathrm{RPP}})/\sigma_\mathcal{V}^{\mathrm{RPP}}$] as a function of Stokes number, Re_λ, and ϕ_v. It is found that, for all experiments, $\sigma_{\mathrm{rel}} > 0$, consistent with the existence of clustering. The most outstanding feature from these figures is the clear dependence of $\sigma_\mathcal{V}$ on the volume fraction, observed in Fig. 9(c), where, for every Reynolds number, σ_{rel} is observed to increase quasilinearly with ϕ_v. Trends with Reynolds and St numbers are more difficult to extract from this simple projection, although Fig. 9(a), where the Reynolds number dependence is encoded in the color of the symbols, suggests an increase of $\sigma_\mathcal{V}$ with St and/or Re_λ.

To further quantify the dependences of σ_{rel} with the three control parameters (St,Re_λ,ϕ_v), power-law fits are computed from the entire experimentally sampled space

$$\sigma_{\mathrm{rel}} = K\, \mathrm{St}^\alpha \mathrm{Re}_\lambda^\beta \phi_v^\gamma. \tag{1}$$

Based on the observations from Fig. 9, we first determine β and γ by a two-variable fit of σ_{rel} as a function of Re_λ and ϕ_v, neglecting the dependence on St in a first approximation. The corresponding data and fit are shown in Fig. 10(a), where the best fit is obtained for $\beta \simeq 0.97 \pm 0.2$ and $\gamma \simeq 0.7 \pm 0.15$. The dependence of σ_{rel} with St is then explored by plotting the compensated quantity $\frac{\sigma_{\mathrm{rel}}}{\mathrm{Re}_\lambda^\beta \phi_v^\gamma}$ as a function of St in Fig. 10(b). The data present very little scatter around a constant value (best power-law fit results in an exponent $\alpha \simeq 0.02 \pm 0.03$). Overall, the dependence of the standard deviation of the Voronoi area distribution on the three controlling parameters (St,Re_λ,ϕ_v) results in
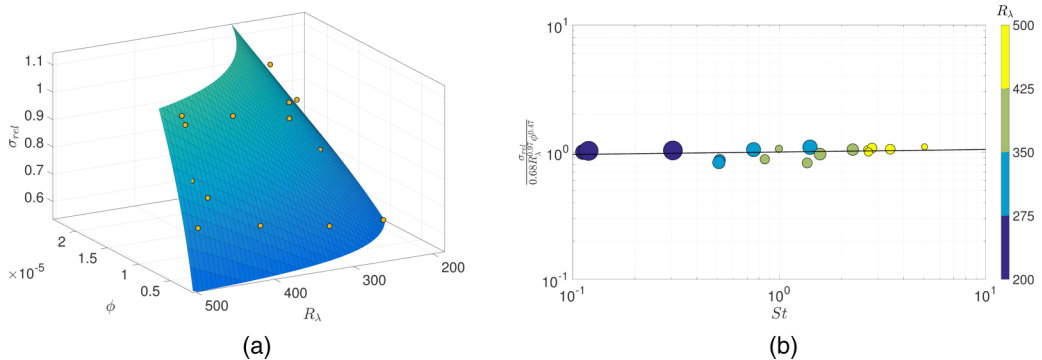
FIG. 10. (a) Plot of σ_{rel} as a function of ϕ_v and Re_λ with a power-law fit $\sigma_{\mathrm{rel}} \propto \mathrm{Re}_\lambda^\beta \phi_v^\gamma$. (b) Plot of σ_{rel} compensated by $\mathrm{Re}_\lambda^\beta \phi_v^\gamma$. The best fit is obtained for $\beta \simeq 0.88$ and $\gamma \simeq 0.5$.

the empirical scaling

$$\sigma_{\mathrm{rel}} = \frac{\sigma_\mathcal{V} - \sigma_\mathcal{V}^{\mathrm{RPP}}}{\sigma_\mathcal{V}^{\mathrm{RPP}}} \simeq 0.68\, \mathrm{St}^{0.02} \mathrm{Re}_\lambda^{0.97} \phi_v^{0.47}. \tag{2}$$

Interestingly, our results point towards a dominant dependence of the clustering on the turbulent Reynolds number, with an intermediate dependence on volume fraction and no dependence on Stokes number.

B. Contribution of clusters and voids to the standard deviation of the Voronoi area distribution

We define clusters and voids in Fig. 8(a), from the thresholds $\mathcal{V}_c$ and $\mathcal{V}_v$ [19,20], corresponding to the points where the experimental Voronoi area PDF is above (more probable than) the RPP. Clusters are defined as particle ensembles with adjacent Voronoi cells whose area $\mathcal{V} < \mathcal{V}_c$, while voids are identified as cells whose area $\mathcal{V} > \mathcal{V}_v$. In the experiments reported here, the two cutoffs are insensitive to flow conditions and their values $\mathcal{V}_c = 0.6$ and $\mathcal{V}_v = 2.1$ are equal to those in previous studies at lower turbulent Reynolds numbers [18,24]. The invariance of these intersections remains to be understood.

The standard deviation $\sigma_\mathcal{V}$ of Voronoi areas represents the second moment of the PDF of $\mathcal{V}$. One can therefore argue that large areas (i.e., voids) contribute more to $\sigma_\mathcal{V}$ than small areas (i.e., clusters). We can indeed write $\sigma_\mathcal{V}^2$ as

$$\sigma_\mathcal{V}^2 = \int_0^{\mathcal{V}_c} (\mathcal{V} - \bar{\mathcal{V}})^2 \mathrm{PDF}(\mathcal{V}) d\mathcal{V} + \int_{\mathcal{V}_c}^{\mathcal{V}_v} (\mathcal{V} - \bar{\mathcal{V}})^2 \mathrm{PDF}(\mathcal{V}) d\mathcal{V} + \int_{\mathcal{V}_v}^{\infty} (\mathcal{V} - \bar{\mathcal{V}})^2 \mathrm{PDF}(\mathcal{V}) d\mathcal{V}, \tag{3}$$

where the three terms give the contribution of clusters, intermediate areas, and voids (denoted by σ_c, σ_i, and σ_v), respectively, to the total standard deviation of Voronoi areas. For the RPP, the three contributions are comparable: $\sigma_c^{\mathrm{RPP}} = 0.29$, $\sigma_v^{\mathrm{RPP}} = 0.30$, and $\sigma_i^{\mathrm{RPP}} = 0.32$. Obviously, $\sigma_c^{\mathrm{RPP}2} + \sigma_i^{\mathrm{RPP}2} + \sigma_v^{\mathrm{RPP}2} = 0.53^2$, as expected. The questions are how these contributions change for inertial particles and how they evolve with the controlling parameters. The experimental data show that σ_v^2 represents on average $\approx 75\%$ (69%–78%, depending on the experimental conditions) of the total variance $\sigma_\mathcal{V}^2$, σ_c^2 is only $\approx 17\%$ (14%–18%), and $\sigma_i^2 \approx 8\%$ (6%–12%). This partition clearly shows a stronger contribution of voids to the total variance compared to clusters, in contrast to the random case, and as expected from the extended tails of the inertial particle Voronoi PDF. The standard deviation of Voronoi areas, as commonly discussed in particle preferential accumulation, is therefore essentially a measure of the distribution of voids. From this point of view, we have analyzed how each of the three contributions—clusters, voids, and intermediate areas—evolves with flow parameters. For each contribution, the relative deviation is compared to the RPP case
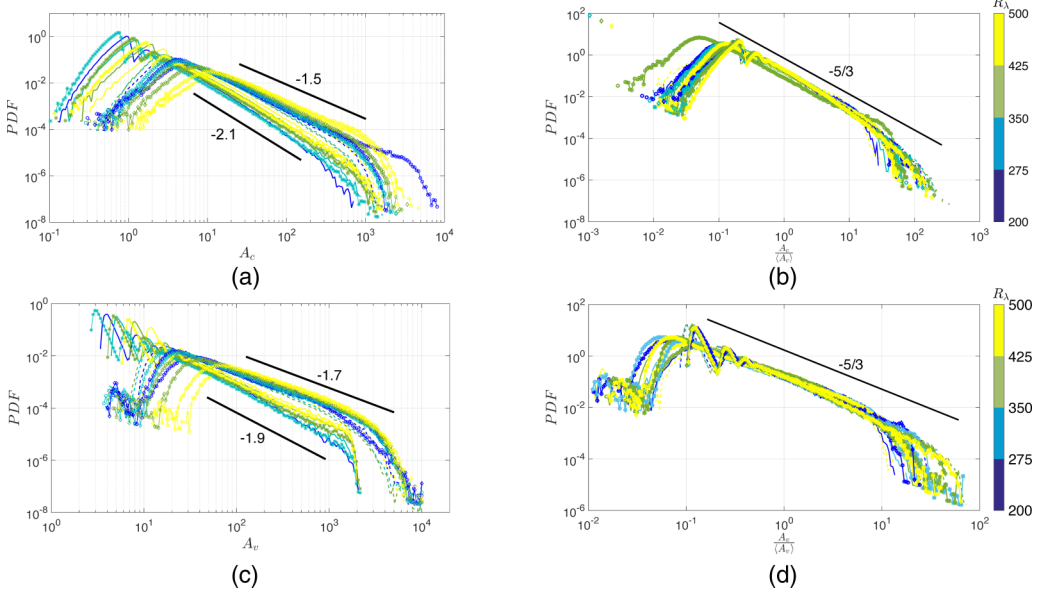
FIG. 11. (a) PDFs of cluster areas A_c and (b) PDFs of cluster areas normalized by the mean. (c) and (d) Same PDFs for the void areas.

$(\sigma_{\mathrm{rel},*} = \frac{\sigma_* - \sigma_*^{\mathrm{RPP}}}{\sigma_*^{\mathrm{RPP}}}$, with $* = c$, i, or v) and their dependences on Reynolds number, Stokes number, and volume fraction are, respectively,

$$\sigma_{\mathrm{rel},c} = 0.11\,\mathrm{Re}_\lambda^{\,1.09\pm0.5}\phi_v^{\,0.43\pm0.25}\mathrm{St}^{-0.06\pm0.06}, \tag{4}$$

$$\sigma_{\mathrm{rel},v} = 0.78\,\mathrm{Re}_\lambda^{\,0.84\pm0.24}\phi_v^{\,0.41\pm0.12}\mathrm{St}^{0.0\pm0.03}, \tag{5}$$

$$\sigma_{\mathrm{rel},i} = 0.35\,\mathrm{Re}_\lambda^{\,0.66\pm0.16}\phi_v^{\,0.35\pm0.08}\mathrm{St}^{-0.03\pm0.07}, \tag{6}$$

These power-law fits show that although the strongest contribution comes indeed from the voids, the dependences on experimental parameters are comparable for all zones, with a leading role for the Reynolds number, a lesser influence of the volume fraction, and practically no dependence on Stokes number, within the range of explored parameters.

C. Geometry of clusters and voids in the particle concentration field

Figure 11 presents the PDF of cluster and void areas, before (left) and after (right) normalization. The cluster PDFs exhibit a distinct peak, indicating the existence of a typical characteristic cluster dimension, in agreement with other previous experimental findings [14,18,24,28]. Figure 11(c) shows that the PDFs of the normalized cluster areas $A_c/\langle A_c\rangle$ follow an algebraic decay with an exponent $n_c \approx -5/3$, for areas larger than the most-probable value. Similar trends are observed for the void areas PDFs, although the range of sizes of the voids is naturally larger than that of the clusters (by a factor about 10). The exponent n_v for the decay of the PDF of normalized void area follows a trend similar to the clusters ($n_v \approx -5/3$). These qualitative features are found to be robust for all experimental conditions. Algebraic decay of the cluster and void areas have been previously reported in several previous experimental and numerical studies [18,19,24,29,30] and is in agreement with a simple model proposed in [30], which predicts an algebraic decay for the PDF of void areas with a $-5/3$ exponent. In this model, the distribution of voids mimics the self-similar distribution of eddies across the turbulent energy cascade, suggesting that clustering (and voiding) of inertial
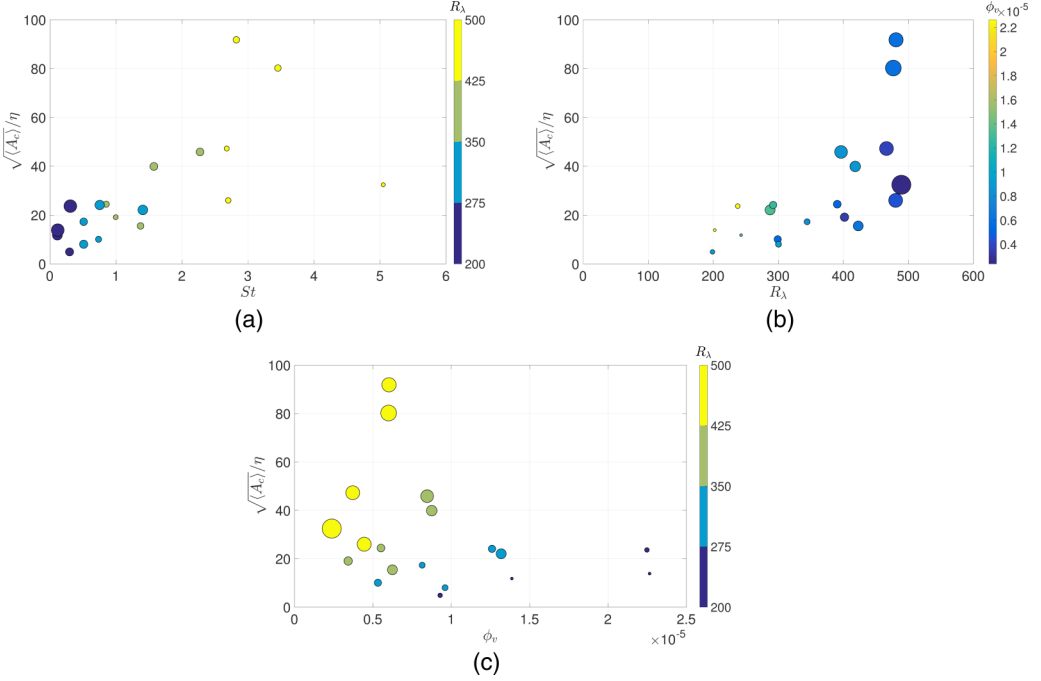
FIG. 12. Dependence of the average cluster size on (a) Stokes number, (b) Reynolds number, and (c) volume fraction. In (a) the color of the symbols indicates the Reynolds number and the size of the symbols reflects the volume fraction. In (b) the color of the symbols indicates the volume fraction and the size of the symbols reflects the Stokes number. In (c) the color of the symbols indicates the Reynolds number and the size of the symbols reflects the Stokes number.

particles is not only driven by small scales but reflects the self-similarity of the carrier turbulence. Unlike in the original work proposing the model, where it applied across the entire spectrum (from η to L_{int}), in these experiments, the $-5/3$ decay holds between a lower length scale between 3η and 10η, depending on flow conditions, and an upper length scale slightly below L_{int}. The largest length scales are not fully resolved in the experiments since the images are about L_{int}, so the tails on the right-hand side of the distributions (Fig. 11) are not statistically significant.

Figure 11 shows that the characteristic cluster size varies with the Reynolds number. Figure 12 quantifies the dependence of $\frac{\sqrt{\langle A_c \rangle}}{\eta}$ on St, Re_λ, and ϕ_v. At first sight, these plots seem to suggest that cluster size increases with increasing Stokes and Reynolds number and decreases with increasing volume fraction. However, as for the previous discussion on σ_V, these trends are complex. Figure 12(a) shows that the increase of $\frac{\sqrt{\langle A_c \rangle}}{\eta}$ with St is very much connected to that in Re_λ (whose value is encoded in the colors of the symbols). Similarly, Figs. 12(b) and 12(c) also point towards a direct connection between trends of $\frac{\sqrt{\langle A_c \rangle}}{\eta}$ and Re_λ and ϕ_v. To obtain better insight into the specific sensitivity to each controlling nondimensional parameter, power-law fits are computed, in the form

$$\frac{\sqrt{\langle A_c \rangle}}{\eta} = K' \text{St}^{\alpha'} \text{Re}_\lambda^{\beta'} \phi_v^{\gamma'}. \tag{7}$$

First, the joint dependences on Re_λ and ϕ_v, shown in Fig. 13(a), are computed. The best fit is obtained for $\beta' = 4.7 \pm 1.5$ and $\gamma' = 1.2 \pm 0.7$. The dependence of cluster size on volume fraction therefore appears to be marginal compared to the Reynolds number dependence. The remaining dependence on St is then probed by fitting the normalized quantity $\frac{\sqrt{\langle A_c \rangle}/\eta}{\text{Re}_\lambda^{4.7}\phi_v^{1.2}}$, shown in Fig. 13(b).
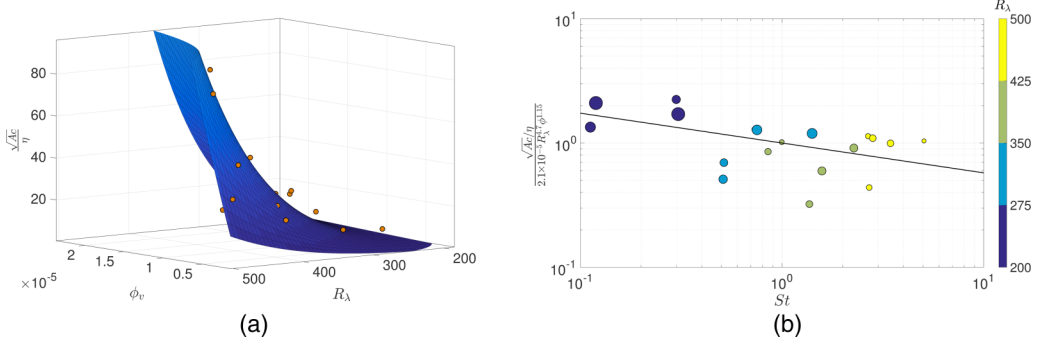
FIG. 13. (a) Scaling of $\frac{\sqrt{\langle A_c \rangle}}{\eta}$ with ϕ_v and R_λ. (b) Reducing the original variable $\frac{\sqrt{\langle A_c \rangle}}{\eta}$ shows the weak dependence on St.

The Stokes-number dependence of the cluster size $\alpha' = -0.24 \pm 0.15$ is relatively weak. Overall, the cluster size dependence on (St, Re_λ, ϕ_v) can be approximately quantified by the empirical expression

$$\frac{\sqrt{\langle A_c \rangle}}{\eta} = (2.1 \times 10^{-5})\mathrm{St}^{-0.25}\mathrm{Re}_\lambda^{4.7}\phi_v^{1.2}, \tag{8}$$

which shows the dominant role of the Reynolds number, a superlinear dependence on volume fraction, and a negligible dependence on Stokes number. This suggests that the cluster size is primarily controlled by the carrier flow turbulence rather than by the disperse phase properties.

Similar trends are also obtained for the size of voids, with sensitivities to Re_λ and to ϕ_v similar to those obtained for the average cluster dimension (see Fig. 14). The Stokes-number dependence is also weak. Since the spatial extension of the void regions is about ten time larger than that of clusters, this ratio carries into the prefactors in Eqs. (8) and (9),

$$\frac{\sqrt{\langle A_v \rangle}}{\eta} = (1.3 \times 10^{-3})\mathrm{St}^{-0.06 \pm 0.1}\mathrm{Re}_\lambda^{3.8 \pm 1.5}\phi_v^{0.98 \pm 0.5}. \tag{9}$$

V. DISCUSSION

Application of Voronoi area statistical analysis to quantifying the geometry of cluster and voids of inertial particles in homogeneous isotropic turbulence has revealed the dependence of the preferential concentration on St, Re_λ, and volume fraction ϕ_v. The standard deviation σ of the distribution of particle Voronoi areas, as well as the length scales of clusters and voids, has a strong dependence
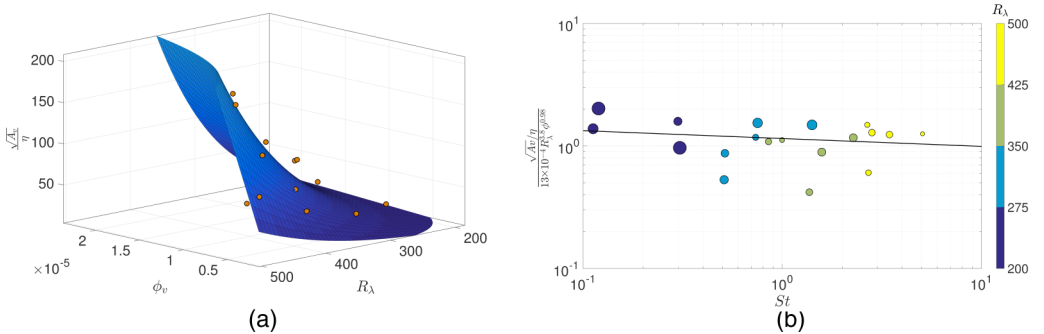

FIG. 14. (a) Scaling of $\frac{\sqrt{\langle A_v \rangle}}{\eta}$ with ϕ_v and R_λ. (b) Reducing the original variable $\frac{\sqrt{\langle A_v \rangle}}{\eta}$ shows the weak dependence on St.

on the Reynolds number, an intermediate dependence on the volume fraction, and no significant dependence (within experimental error) on the Stokes number. This strong dependence of clustering on the Re_λ reveals the dominant role of carrier flow turbulence in the clustering process, consistent with the assumption that the turbulent structures are the ones responsible for the formation of clusters.

The dependence of clustering on the particle volume fraction ϕ_v is reminiscent of collective effects due to particle interactions and is in agreement with previous observations of such collective effects [14,19]. A very weak, almost nonexistent, dependence of cluster geometry on the Stokes number, based on the maximum probability diameter in the polydisperse particle distributions used in these experiments, has been found. It has been consistently reported from studies of monodisperse particle-laden flows [12,31–33] that clustering is maximum for Stokes number of order unity, invoking a better resonance between particle response time and small turbulent eddies. Most metrics used to characterize the level of clustering are based on small-scale quantities, for instance, the correlation dimension that measures the increase of probability of finding two particles at vanishing distance compared to a random distribution. Such metrics are only relevant to quantify small-scale clustering at subdissipative scales, which has been shown to be driven by Reynolds number and to be essentially independent of Stokes number [33]. This analysis is very different from that used in experiments with metrics that focus on inertial scales (most accessible Voronoi cells in experiments, such as the one shown in Fig. 7, have dimensions within the inertial range of scales). In line with previous numerical studies [29,30,33], our experimental results point towards clustering of inertial particles being not only a small-scale phenomenon, but one that occurs at all scales of turbulence. This is revealed, for instance, by the algebraic decay of the PDF of cluster areas and by the fact that average cluster dimensions, up to 100η, can be found for experiments at the highest Reynolds numbers. The importance of multiscale clustering has also been recently emphasized by Coleman and Vassilicos [3], who showed that the usual centrifugation mechanism [1], which is by essence a small-scale preferential clustering mechanism based on the negative effective compressibility of high-strain–low-vorticity regions of the carrier turbulence, is not the primary mechanism for preferential concentration of particles in turbulence when the Stokes number exceeds unity. Their numerical study shows that for particles with Stokes number larger than unity, clustering is primarily driven by the sweep-stick mechanism [3] by which particles tend to preferentially sample the zero-acceleration points of the carrier flow. It is important to note that, contrary to the centrifugation mechanism, which is indeed a clustering mechanism, the sweep-stick mechanism is a preferential sampling mechanism and clustering only emerges as a consequence of the low-acceleration points in a turbulent flow organizing in multiscale clusters [30]. In this framework, clustering properties are driven by turbulence characteristics across scales, while particle properties only influence the ability of particles to preferentially stick to the aforementioned zero-acceleration points. The main constraint for particles to efficiently stick to zero-acceleration points is that their viscous relaxation time τ_p be small compared to the lifetime of those zero-acceleration points. These points are known from numerical simulations to be very persistent [30] and this can be related to the experimental finding that the correlation time of the acceleration magnitude of tracer particles is of the order of the integral time scale T_{int} of the carrier turbulence [34]. As a consequence, as long as $\tau_p \ll T_{int}$, no significant dependence of clustering by the sweep-stick mechanism on the Stokes number is expected. A significant decrease of the efficiency of the mechanism will only occur for particles with response times approaching the integral time scale of the flow. In our experiment, T_{int} is at least of the order of 100 ms or more. For water droplets, such high response times would require particles with diameter of the order of 100 μm or more. Interestingly, the sweep-stick scenario also suggests that the impact of Stokes number should be more visible at lower Reynolds number as the condition St $\ll T_{int}/\tau_\eta$ becomes more stringent for lower Reynolds numbers. This may explain why, in low-Reynolds-number simulations [12], where $R_\lambda \approx 30$, and experiments [19], a decrease of clustering was indeed observed when the Stokes number exceeds unity.

Finally, we also point out that the polydispersity of our droplet distribution would also be very likely to smear out possible weak Stokes-number dependences, in particular for the experiments at the lowest Reynolds numbers for which some dependence may still have been expected. Monchaux has

addressed several possible biases, including the effect of polydispersity, on clustering diagnoses [35]. By combining numerical data from [36], where inertial particles dynamics is investigated for different Stokes numbers in turbulence at $R_\lambda \approx 200$, he has shown indeed that for St $\gtrsim 1$, the dependence of the standard deviation of Voronoi areas on Stokes number (which is already small for the monodisperse situation) is further reduced (see Fig. 6 in [35]) when particles at different Stokes numbers are mixed.

The sensitivity of clustering to the volume fraction identified here is clearly beyond any measurement uncertainty. If, as discussed above, the sweep-stick mechanism is driving the cluster formation, any volume fraction influence is not captured in that picture. A possible scenario could rely on collective effects that are known to lead to denser regions sinking in the mixture with an enhanced settling velocity. Such denser regions could thus collect extra particles during their motion relative to the fluid and therefore built up clusters of higher concentration and of larger size. Such a process would be clearly favored at higher volume fractions. In this scenario, the sweep-stick mechanism will act as the trigger of cluster formation, with subsequent growth driven by the collective dynamics. Another alternative view is that the presence of clusters modifies the local turbulent structure and favor the multiplication of sticking points in the flow (note that at the largest concentrations in clusters, the mass loading exceeds 0.1 and can even become close to unity): More particles could then either *activate* more zero acceleration points or help bring new particles in the sticking region. These scenarios, hypothetical as they are, may serve for planing new experiments to help understand how collective effects become efficient in clustering. Clearly, an investigation of the effect of disperse phase volume fraction on the microscale mechanism for accumulation of particles would be worth undertaking.

VI. CONCLUSION

Overall, our findings of a dominant role of the Reynolds number compared to the Stokes number is consistent with a leading multiscale clustering process driven by a preferential sampling mechanism, such as the sweep-stick mechanism, in agreement with previous experimental results [18]. In a broader framework, this finding also supports the necessity to distinguish small-scale mechanisms of clustering and multiscale mechanisms [37].

The investigation of clustering in regard to its effect on settling of inertial particles is another important aspect that can be studied via conditioned joint statistics of settling velocity and Voronoi analysis. This study should ideally provide the dependence of the settling velocity of inertial particles on turbulence fluctuations and a final expression for the connection between settling and clustering.

We finish by emphasizing that, due to intertwining of all three control parameters St, Re_λ, and ϕ_v, the separation of their influence on clustering is an extremely difficult task. More experiments need to be conducted to extend quantitative understanding to a broader range of parameter values, in particular regarding the role of volume fraction and collective effects.

---

[1] M. Maxey, The gravitational settling of aerosol-particles in homogeneous turbulence and random flow-fields, J. Fluid Mech. **174**, 441 (1987).

[2] S. Goto and J. C. Vassilicos, Sweep-Stick Mechanism of Heavy Particle Clustering in Fluid Turbulence, Phys. Rev. Lett. **100**, 054503 (2008).

[3] S. W. Coleman and J. C. Vassilicos, A unified sweep-stick mechanism to explain particle clustering in two- and three-dimensional homogeneous, isotropic turbulence, Phys. Fluids **21**, 113301 (2009).

[4] N. M. Qureshi, M. Bourgoin, C. Baudet, A. Cartellier, and Y. Gagne, Turbulent Transport of Material Particles: An Experimental Study of Finite Size Effects, Phys. Rev. Lett. **99**, 184502 (2007).

[5] N. M. Qureshi, U. Arrieta, C. Baudet, A. Cartellier, Y. Gagne, and M. Bourgoin, Acceleration statistics of inertial particles in turbulent flow, Eur. Phys. J. B **66**, 531 (2008).

[6] H. Xu and E. Bodenschatz, Motion of inertial particles with size larger than Kolmogorov scale in turbulent flows, Physica D **237**, 2095 (2008).

[7] F. Lucci, A. Ferrante, and S. Elghobashi, Is Stokes number an appropriate indicator for turbulence modulation by particles of Taylor-length-scale size?, Phys. Fluids **23**, 025101 (2011).

[8] H. Homann and J. Bec, Finite-size effects in the dynamics of neutrally buoyant particles in turbulent flow, J. Fluid Mech. **651**, 81 (2010).

[9] L. Fiabane, R. Zimmermann, R. Volk, J.-F. Pinton, and M. Bourgoin, Clustering of finite-size particles in turbulence, Phys. Rev. E **86**, 035301 (2012).

[10] T. Doychev and M. Uhlmann, in *Proceedings of the Seventh International Conference on Multiphase Flow*, edited by S. Balachandar and J. S. Curtis (University of Florida Press, Gainesville, 2010).

[11] J. C. Vassilicos, Dissipation in turbulent flows, Annu. Rev. Fluid Mech. **47**, 95 (2015).

[12] L. P. Wang and M. R. Maxey, Settling velocity and concentration distribution of heavy particles in homogeneous isotropic turbulence, J. Fluid Mech. **256**, 27 (1993).

[13] C. Y. Yang and U. Lei, The role of the turbulent scales in the settling velocity of heavy particles in homogeneous isotropic turbulence, J. Fluid Mech. **371**, 179 (1998).

[14] A. Aliseda, A. Cartellier, F. Hainaux, and J. C. Lasheras, Effect of preferential concentration on the settling velocity of heavy particles in homogeneous isotropic turbulence, J. Fluid Mech. **468**, 77 (2002).

[15] G. T. Csanady, Turbulent diffusion of heavy particles in the atmosphere, J. Atmos. Sci. **20**, 201 (1963).

[16] M. R. Wells and D. E. Stock, The effect of crossing trajectories on the dispersion of particles in a turbulent flow, J. Fluid Mech. **136**, 31 (1983).

[17] M. R. Maxey and J. J. Riley, Equation of motion for a small rigid sphere in a nonuniform flow, Phys. Fluids **26**, 883 (1983).

[18] M. Obligado, T. Teitelbaum, A. Cartellier, P. D. Mininni, and M. Bourgoin, Preferential concentration of heavy particles in turbulence, J. Turbul. **15**, 293 (2014).

[19] R. Monchaux, M. Bourgoin, and A. Cartellier, Preferential concentration of heavy particles: A Voronoi analysis, Phys. Fluids **22**, 103304 (2010).

[20] R. Monchaux, M. Bourgoin, and A. Cartellier, Analyzing preferential concentration and clustering of inertial particles in turbulence, Int. J. Multiphase Flow **40**, 1 (2012).

[21] H. Makita and K. Sassa, in *Advances in Turbulence 3*, edited by A. V. Johansson and P. K. Alfredsson (Springer, Berlin, 1991), pp. 497–505.

[22] L. Mydlarski and Z. Warhaft, On the onset of high-Reynolds-number grid-generated wind tunnel turbulence, J. Fluid Mech. **320**, 331 (1996).

[23] R. Poorte and A. Biesheuvel, Experiments on the motion of gas bubbles in turbulence generated by an active grid, J. Fluid Mech. **461**, 127 (2002).

[24] M. Obligado, A. Cartellier, and M. Bourgoin, Experimental detection of superclusters of water droplets in homogeneous isotropic turbulence, Europhys. Lett. **112**, 54004 (2015).

[25] J.-S. Ferenc and Z. Neda, On the size distribution of Poisson Voronoi cells, Physica A **385**, 518 (2007).

[26] Y. Tagawa, J. Martínez Mercado, V. N. Prakash, E. Calzavarini, C. Sun, and D. Lohse, Three-dimensional Lagrangian Voronoï analysis for clustering of particles and bubbles in turbulence, J. Fluid Mech. **693**, 201 (2012).

[27] M. Uhlmann and T. Doychev, Sedimentation of a dilute suspension of rigid spheres at intermediate Galileo numbers: The effect of clustering upon the particle motion, J. Fluid Mech. **752**, 310 (2014).

[28] C. P. Bateson and A. Aliseda, Wind tunnel measurements of the preferential concentration of inertial droplets in homogeneous isotropic turbulence, Exp. Fluids **52**, 1373 (2012).

[29] G. Boffetta, F. De Lillo, and A. Gamba, Large scale inhomogeneity of inertial particles in turbulent flows, Phys. Fluids **16**, L20 (2004).

[30] S. Goto and J. C. Vassilicos, Self-similar clustering of inertial particles and zero-acceleration points in fully developed two-dimensional turbulence, Phys. Fluids **18**, 115103 (2006).

[31] J. R. Fessler, J. D. Kulick, and J. K. Eaton, Preferential concentration of heavy particles in a turbulent channel flow, Phys. Fluids **6**, 3742 (1994).

[32] J. Bec, L. Biferale, G. Boffetta, A. Celani, M. Cencini, A. Lanotte, S. Musacchio, and F. Toschi, Acceleration statistics of heavy particles in turbulence, J. Fluid Mech. **550**, 349 (2006).

[33] J. Bec, L. Biferale, M. Cencini, A. Lanotte, S. Musacchio, and F. Toschi, Heavy Particle Concentration in Turbulence at Dissipative and Inertial Scales, Phys. Rev. Lett. **98**, 084502 (2007).

[34] N. Mordant, J. Delour, E. Léveque, A. Arnéodo, and J.-F. Pinton, Long Time Correlations in Lagrangian Dynamics: A Key to Intermittency in Turbulence, Phys. Rev. Lett. **89**, 254502 (2002).

[35] R. Monchaux, Measuring concentration with Voronoï diagrams: The study of possible biases, New J. Phys. **14**, 095013 (2012) .

[36] H. Yoshimoto and S. Goto, Self-similar clustering of inertial particles in homogeneous turbulence, J. Fluid Mech. **577**, 275 (2007).

[37] K. Gustavsson and B. Mehlig, Statistical models for spatial patterns of heavy particles in turbulence, Adv. Phys. **65**, 1 (2016).